

## Phase retrieval of the full vectorial field applied to coherent Fourier scatterometry

Xu, Xiaosi; Konijnenberg, A. P.; Pereira, S. F.; Urbach, H. P.

**DOI**

[10.1364/OE.25.029574](https://doi.org/10.1364/OE.25.029574)

**Publication date**

2017

**Document Version**

Final published version

**Published in**

Optics Express

**Citation (APA)**

Xu, X., Konijnenberg, A. P., Pereira, S. F., & Urbach, H. P. (2017). Phase retrieval of the full vectorial field applied to coherent Fourier scatterometry. *Optics Express*, 25(24), 29574-29586.  
<https://doi.org/10.1364/OE.25.029574>

**Important note**

To cite this publication, please use the final published version (if applicable).  
Please check the document version above.

**Copyright**

Other than for strictly personal use, it is not permitted to download, forward or distribute the text or part of it, without the consent of the author(s) and/or copyright holder(s), unless the work is under an open content license such as Creative Commons.

**Takedown policy**

Please contact us and provide details if you believe this document breaches copyrights.  
We will remove access to the work immediately and investigate your claim.



# Phase retrieval of the full vectorial field applied to coherent Fourier scatterometry

XIAOSI XU, A. P. KONIJNENBERG, S. F. PEREIRA,\* AND H. P. URBACH

*Dept. of Imaging Physics, Faculty of Applied Sciences, Delft University of Technology, Lorentzweg 1, 2628CJ Delft, The Netherlands*

\**s.f.pereira@tudelft.nl*

**Abstract:** Coherent Fourier scatterometry is an optical metrology technique that utilizes the measured intensity of the scattered optical field to reconstruct certain parameters of test structures written on a wafer with nano-scale accuracy. The intensity of the scattered field is recorded with a camera and this information is used to retrieve the grating parameters. To improve sensitivity in the parameter reconstruction, the phase of the scattered field can also be acquired. Interferometry can be used for this purpose, but with the cost of cumbersomeness. In this paper, we show that iterative phase retrieval methods can be applied to retrieve the scattered complex fields from only intensity measurement data. We show that the accuracy of the retrieved complex fields using phase retrieval is comparable to that measured directly using interferometry.

© 2017 Optical Society of America

**OCIS codes:** (050.2770) Gratings; (070.0070) Fourier optics and signal processing; (100.5070) Phase retrieval; (120.3940) Metrology; (120.4630) Optical inspection.

## References and links

1. O. El Gawhary, N. Kumar, S. F. Pereira, W. M. J. Coene, and H. P. Urbach, "Performance analysis of coherent optical scatterometry," *Appl. Phys. B* **105**(4), 775–781 (2011).
2. N. Kumar, O. el Gawhary, S. Roy, S. F. Pereira, and H. P. Urbach, "Phase retrieval between overlapping orders in coherent Fourier scatterometry using scanning," *J. Eur. Opt. Soc. Rapid Publ.* **8**, 13048 (2013).
3. S. Roy, N. Kumar, S. F. Pereira, and H. P. Urbach, "Interferometric coherent Fourier scatterometry: a method for obtaining high sensitivity in the optical inverse-grating problem," *J. Opt.* **15**(7), 075707 (2013).
4. C. Falldorf, M. Agour, C. Von Kopylow, and R. B. Bergmann, "Phase retrieval for optical inspection of technical components," *J. Opt.* **14**(16), 065701 (2012).
5. M. Agour, P. Almoró, and C. Falldorf, "Investigation of smooth wave fronts using SLM-based phase retrieval and a phase diffuser," *J. Eur. Opt. Soc. Rapid Publ.* **7**, 12046 (2012).
6. M. Agour, C. Falldorf, and R. B. Bergmann, "Investigation of composite materials using SLM-based phase retrieval," *Opt. Lett.* **38**(13), 2203–2205 (2013).
7. A. Alpers, G. T. Herman, H. F. Poulsen, and S. Schmidt, "Phase retrieval for superposed signals from multiple objects," *J. Opt. Soc. Am. A* **27**(9), 1927–1937 (2010).
8. J. Gulden, O. M. Yefanov, A. P. Mancuso, R. Dronyak, A. Singer, V. Bernátová, A. Burkhardt, O. Polozhentsev, A. Soldatov, M. Sprung, and I. A. Vartanyants, "Three dimensional structure of a single colloidal crystal strain studied by coherent x-ray diffraction," *Opt. Express* **20**(4), 4039–4049 (2012).
9. J. C. Petrucci, L. Tian, and G. Barbastathis, "The transport of intensity equation for optical path length recovery using partially coherent illumination," *Opt. Express* **21**(12), 14430–14441 (2013).
10. H. H. Bauschke, J. M. Borwein, "On the convergence of von Neumann's alternating projection algorithm for two sets," *Set-Valued Anal.* **1**(2), 185–212 (1993).
11. J. R. Fienup, "Phase retrieval algorithms: a comparison," *Appl. Opt.* **21**(15), 2758–2769 (1982).
12. R. W. Gerchberg and W. O. Saxton, "A practical algorithm for the determination of phase from image and diffraction plane pictures," *Optik* **35**(2), 237–246 (1972).
13. S. Marchesini, "Invited article: A unified evaluation of iterative projection algorithms for phase retrieval," *Rev. Sci. Instrum.* **78**(1), 011301 (2007).
14. D. E. Adams, L. S. Martin, M. D. Seaberg, D. F. Gardner, H. C. Kapteyn, and M. M. Murnane, "A generalization for optimized phase retrieval algorithms," *Opt. Express* **20**(22), 24778–24790 (2012).
15. V. Elser, "Phase retrieval by iterated projections," *J. Opt. Soc. Am. A* **20**(1), 40–55 (2003).
16. N. Kumar, L. Cisotto, S. Roy, G. K. P. Ramanandan, S. F. Pereira, and H. P. Urbach, "Determination of the full scattering matrix using coherent Fourier scatterometry," *Appl. Opt.* **55**(16), 4408–4413 (2016).
17. D. R. Luke, "Relaxed averaged alternating reflections for diffraction imaging," *Inverse Probl.* **21**(1), 37–50 (2004).

18. A. V. Martin, F. Wang, N. D. Loh, T. Ekeberg, F. R. N. C. Maia, M. Hantke, G. van der Schot, C. Y. Hampton, R. G. Sierra, A. Aquila, S. Bajt, M. Barthelmess, C. Bostedt, J. D. Bozek, N. Coppola, S. W. Epp, B. Erk, H. Fleckenstein, L. Foucar, M. Frank, H. Graafsma, L. Gumprecht, A. Hartmann, R. Hartmann, G. Hauser, H. Hirsemann, P. Holl, S. Kassemeyer, N. Kimmel, M. Liang, L. Lomb, S. Marchesini, K. Nass, E. Pedersoli, C. Reich, D. Rolles, B. Rudek, A. Rudenko, J. Schulz, R. L. Shoeman, H. Soltau, D. Starodub, J. Steinbrener, F. Stellato, L. Strüder, J. Ullrich, G. Weidenspointner, T. A. White, C. B. Wunderer, A. Barty, I. Schlichting, M. J. Bogan, and H. N. Chapman, "Noise-robust coherent diffractive imaging with a single diffraction pattern," *Opt. Express* **20**(15), 16650–16661 (2012).
19. J. A. Rodriguez, R. Xu, C. C. Chen, Y. Zou, and J. Miao, "Oversampling smoothness: an effective algorithm for phase retrieval of noisy diffraction intensities," *J. Appl. Crystallogr.* **46**(2), 312–318 (2013).
20. J. R. Fienup and C. C. Wackerman, "Phase-retrieval stagnation problems and solutions," *J. Opt. Soc. Am. A* **3**(11), 1897–1907 (1986).
21. A. P. Konijnenberg, W. M. J. Coene, S. F. Pereira, and H. P. Urbach, "Combining ptychographical algorithms with the Hybrid-Output (HIO) algorithm," *Ultramicroscopy* **171**, 43–54 (2016).

## 1. Introduction

Optical scatterometry is widely used in the semiconductor industry to retrieve parameters of gratings written on wafers in order to test the quality of the photolithographic process. Currently, the so called incoherent Fourier scatterometry (IFS) is used for this purpose. In this case, incoherent light is incident on the grating and the intensity of the scattered orders that are captured by the lens are measured and used for the reconstruction of parameters of the gratings. Recently, Coherent Fourier scatterometry (CFS) has been proposed [1], where a coherent light source is focused on the grating, and the zeroth and possibly also higher orders of the reflected light are captured by the same objective and the intensity of the far field is recorded. If the period of the grating is such that more orders are captured by the objective, interference occurs between the various orders. By scanning the grating w.r.t. the focused spot, it is possible to determine the phase differences between the orders [2], and this additional information helps in the parameter retrieval problem. However, when the grating has a period that is so small that only the  $0^{th}$  order but no higher reflected orders are captured by the objective, the advantage of CFS over IFS is lost. Thus, in the case of non overlapping orders at the pupil, one can gain extra information by measuring not only the intensity but also the phase of the entire scattered field, for example, by interfering the scattered field with a reference beam. In [3], it was shown that knowledge of the phase improves the sensitivity of CFS, so that its applicability can be extended to gratings with small periods. As mentioned before, interferometry would be a straightforward method to obtain the phase in this case, but it has disadvantages since it requires a complicated setup that is sensitive to environmental vibrations. Another option is to use phase retrieval methods where only intensity measurements are required.

Phase retrieval is a well developed technique which is widely used in fields of applied physics and engineering [4–8]. Over the years, many approaches have been reported for the phase retrieval problem, including the transport of intensity equation [9], which solved the propagation equation of the electromagnetic field in different planes along the optical axis, and the most popular alternating projection methods [10]. Most of the present existing alternating projection algorithms have been developed in the pioneering work of Fienup [11] and Gerchberg and Saxton [12]. Both of these works are based on an iteration between two intensity patterns related to each other by propagation. Most of the approaches require prior knowledge which are used as constraints, and even with such knowledge there is no guarantee for uniqueness of the solution, as the algorithm can stagnate in a local minimum. However, other more stable approaches have been proposed which has broadened applications in numerous fields [13, 14].

Phase retrieval based on iterative projections are the most commonly used and broadly developed methods. Iterations are expressed as projections onto sets, which are defined by the support in the object domain and the modulus of the field in the Fourier domain [13, 15]. Generally, iterative algorithms modify the object in each cycle to approach the solution which

satisfies the support constraint in the object domain and the modulus constraint in the Fourier domain. In this paper, iterative phase retrieval methods were applied to retrieve the complex vectorial field (which is equivalent to the scattered far field) in the exit pupil of the objective. We compared the retrieved amplitude and phase with the experimental result which was previously obtained with an interferometer and the theoretically expected far field obtained by rigorous electromagnetic simulations.

The paper is organised as follows: firstly in section 2 we will briefly introduce the phase retrieval algorithms that we have used to retrieve the phase of the far field. In section 3, we will present simulations applied with these algorithms to retrieve the phase and amplitude of the scattered far field of a sub-wavelength grating illuminated by a focused laser beam. Then in section 4 the retrieved field from measurement data will be shown and compared with results obtained from interferometric data and also from simulations (previously reported in [16]). Finally we will conclude our discoveries in section 5.

## 2. Phase retrieval theory

Several iterative methods use the relation between the object domain and Fourier domain via Fourier transforms. We use  $f(x, y)$  and  $F(u, v)$  to represent respectively the object field and diffraction field that can be written in terms of amplitude and phase as:  $f(x, y) = |f(x, y)|e^{i\psi(x, y)}$ ,  $F(u, v) = |F(u, v)|e^{i\theta(u, v)}$ . The challenge here is to retrieve either the phase  $\psi(x, y)$  or  $\theta(u, v)$  from intensity measurements on both planes or on the diffraction plane alone. In this paper, different algorithms including the hybrid-input-output (HIO), relaxed averaged alternating reflections (RAAR), modified HIO (M-HIO), oversampling smoothness (OSS) algorithms are applied for our phase retrieval simulation. Presently, it is useful to begin by giving a brief explanation of these algorithms.

### 2.1. Hybrid input output method (HIO)

The hybrid input output algorithm [11] uses a support constraint (i.e. prior knowledge of the shape of the object  $f(x, y)$ ) and an intensity measurement  $|F(u, v)|^2$  in the Fourier domain to reconstruct the object, where  $F(u, v)$  represents the Fourier transform of  $f(x, y)$ . Note that even though one tends to speak of ‘an object’ that is reconstructed when discussing these algorithms, in our particular case this refers to the pupil field we want to reconstruct. This approach does iterative projections between the Fourier and object domains through the following process (in the  $k^{\text{th}}$  iteration):

1. We have an object estimate  $f_k(x, y)$ ;
2. Fourier transform  $f_k(x, y)$  to get the estimated diffraction field  $F_k(u, v)$ ;
3. Replace the amplitude of  $F_k(u, v)$  with the measured amplitude  $|F(u, v)|$  while keeping the phase to obtain the updated estimated field  $F'_k(u, v)$ ;
4. Inverse Fourier transform the updated estimated diffracted field  $F'_k(u, v)$ , which gives  $f'_k(x, y)$ ;
5. Apply the support constraint in the object domain to obtain the object  $f_k(x, y)$

$$f_{k+1}(x, y) = \begin{cases} f'_k(x, y) & (x, y) \notin \gamma \\ f_k(x, y) - \beta f'_k(x, y) & (x, y) \in \gamma, \end{cases} \quad (1)$$

where  $\gamma$  is the set of points where the support constraint in the object domain is violated, i.e. we know a priori that  $f(x, y) = 0$  for  $(x, y) \in \gamma$ .  $\beta$  is a feedback factor which is between 0 and 1.

## 2.2. Relaxed averaged alternating reflections (RAAR)

The relaxed averaged alternating reflections algorithm has a relaxed shift of the field in the object domain [17]. Compared with HIO, the only difference of RAAR is the following operation in the object domain:

$$f_{k+1}(x, y) = \begin{cases} f'_k(x, y) & (x, y) \notin \gamma \\ \beta f_k(x, y) + (1 - 2\beta)f'_k(x, y) & (x, y) \in \gamma. \end{cases} \quad (2)$$

## 2.3. Modified HIO (M-HIO)

The modified HIO algorithm [18] is the revision of HIO that aims at filtering the signals that are likely to be noises, so as to increase the robustness of HIO in the case with noisy measurement data. It is suggested that the reconstructed phase error and environmental noise comprise the error outside the support:

$$f_k = f_{k\_error} + \sigma_{noise}, \quad (3)$$

where  $f_{k\_error}$  is the retrieval error. The ratio of  $f_{k\_error}/\sigma_{noise}$  is defined as the effective signal to noise ratio  $\varepsilon$ . By choosing a reasonable  $\varepsilon$  when applying the object constraint, one can expect to increase the robustness of the algorithm. A reliable approximation can be 2, i.e.  $f_{k\_error} \approx 2\sigma_{noise}$ , in which case the object plane constraint in the HIO algorithm is modified with the form:

$$f_{k+1}(x, y) = \begin{cases} f'_k(x, y) & (x, y) \notin \gamma \\ f_k(x, y) - \beta f'_k(x, y) & (x, y) \in \gamma \quad \& \quad |f'_k(x, y)| > 3\sigma_{noise} \\ 0 & (x, y) \in \gamma \quad \& \quad |f'_k(x, y)| \leq 3\sigma_{noise}. \end{cases} \quad (4)$$

## 2.4. Oversampling smoothness method (OSS)

The oversampling smoothness method [19] deals with noisy measurement of diffraction data by applying a spatial frequency filter in the Fourier domain. Compared with the HIO algorithm, it introduces an additional constraint in the real space by convolution of the Fourier transform of the estimate object with an adaptive Gaussian filter. The first part of an iteration with OSS is the same as that with HIO as explained above. However, after applying the support constraint to obtain

$$f''_k(x, y) = \begin{cases} f'_k(x, y) & (x, y) \notin \gamma \\ f_k(x, y) - \beta f'_k(x, y) & (x, y) \in \gamma, \end{cases} \quad (5)$$

spatial frequency filter is applied:

$$f_{k+1}(x, y) = \begin{cases} f''_{k+1}(x, y) & (x, y) \notin \gamma \\ \mathcal{F}^{-1}\{F''_k(u, v) \cdot W(u, v)\} & (x, y) \in \gamma, \end{cases} \quad (6)$$

where  $F''_k(u, v)$  is the Fourier transform of  $f''_k(x, y)$ ,  $\mathcal{F}^{-1}\{\cdot\}$  refers to the inverse Fourier transform, and  $W(u, v)$  is the normalized Gaussian function:

$$W(u, v) = e^{-0.5 \frac{u^2+v^2}{(w\alpha_o)^2}}, \quad (7)$$

where  $\alpha_o$  is a constant and  $w$  is the weighing factor. OSS is applied with 10 steps, and the weighing factor  $w$  changes in each step, from  $N$  to  $N/10$ , where  $N$  is the array size of the domain. The Gaussian function applied here filters more signals from high frequency patterns than from low frequency patterns, and this filtering effect diminishes as the iteration goes until the algorithm finds a solution. This method is reported to have higher robustness than HIO and ER algorithms to retrieve images from noisy measurement data and is effective to avoid stagnation around a local minimum.

### 3. Simulation

In this section we apply the methods described in Section 2 to retrieve the amplitude and phase of the reflected far field of a periodic grating structure. Figure 1 shows the schematic view of the setup. A polarized and collimated laser beam passes through a beam splitter and is focused on the sample by lens 2. The back-reflected light from the sample is reflected by the beam splitter and passes through a second polarizer followed by lens 3 which focuses the light on the detector. Lens 3 is in the position such that the field in the detector plane is the Fourier transform of the field in the back focal plane (BFP) of lens 2, making the two fields to be a Fourier transform pair. The intensities of both the fields were simulated and different algorithms were applied to retrieve the phase of the field in the BFP of lens 2.

Figure 2 shows the schematic view of a silicon grating, which is commonly used in characterizations for lithography inspection purposes. The sample can be described by four parameters: period, height, critical dimension at the half height (midCD) and side wall angle (SWA): while by design the grating should be a shape of cuboid bars, the upper part of the bar in practice is normally etched more than the lower part due to fabrication imperfection, making the cross section of the bars to be a trapezoid. Here in this paper we used a grating with period of 500 nm, height of 130 nm, midCD of 216 nm, SWA of 85 degrees and numerical aperture of lens 2 to be 0.4. The wavelength of the laser applied was 633 nm.

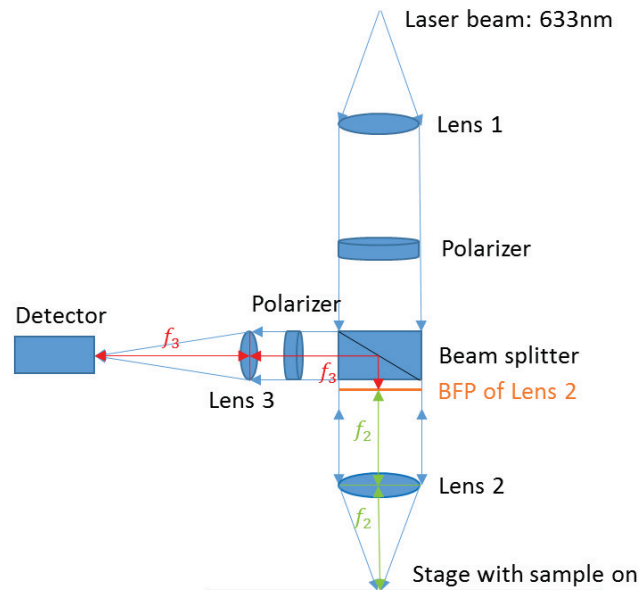


Fig. 1. Schematic overview of the setup used both in simulation and experiment.

In order to obtain more information of the far field, polarization was also considered. Two polarization directions were applied at the entrance and exit pupils of the optical system; the incident light was linearly polarized with the polarization axis perpendicular (TM) to the grating structure, while the polarization direction before lens 3 can be perpendicular (TE) or parallel (TM) to the input polarization. In this way two different polarization combinations were obtained, namely TMTE and TMTM. For the simulations below, we focus on the retrieval of field in the TMTM case, which shows a rich phase distribution over the entire far field.

The phase retrieval algorithms including HIO, OSS, M-HIO and RAAR and some combinations

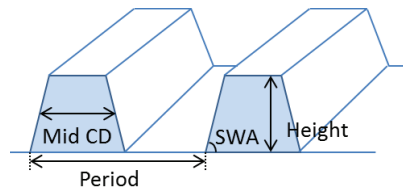


Fig. 2. Schematic overview of the structure of the grating

of these algorithms were employed. In order to have a realistic view of the performance of different algorithms, Poisson noise and white Gaussian noise with a SNR of 100 were added to the intensity pattern in the diffraction plane. The initial object estimate is chosen to have a constant amplitude and phase inside the support region. It is known that if the support and the intensity pattern are both centrosymmetric, this initial guess will lead the algorithm to fail [12]. Even though in the ideal case for our application the intensity pattern would indeed be centrosymmetric, in the simulations and in the experiments this symmetry is broken due to noise and imperfections in the setup, and with trial and error we observed that in this case, choosing a constant phase for the initial object estimate yielded a lower reconstruction error than a random phase. The  $\beta$  values used here were 0.7 for the HIO, M-HIO and OSS algorithms and 0.96 for RAAR (also for the combined ones), respectively. For the combined algorithms, HIO was applied for the first 150 cycles, followed by the second algorithm for the last 450 cycles. In order to avoid the twin image stagnation problem, an asymmetrical mask was applied in the first several cycles, as suggested in [20]. Also, the support constraint we used ( $60 \times 60$  pixels) was slightly larger than the actual support ( $54 \times 54$  pixels), as suggested in [11].

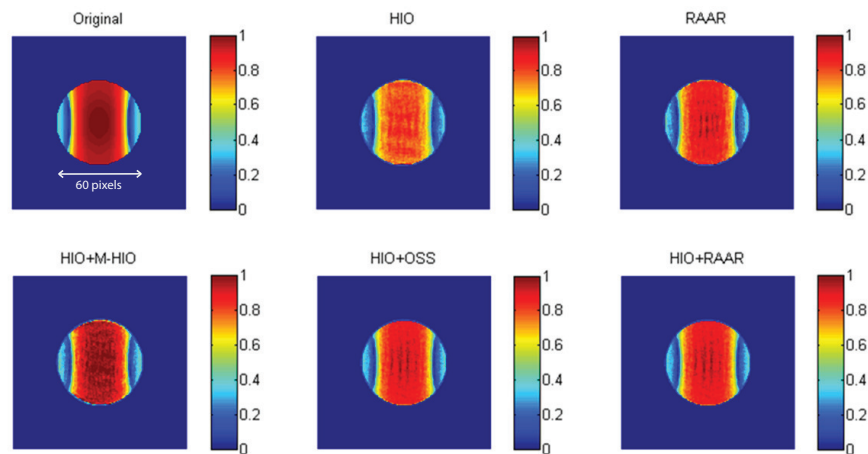


Fig. 3. The original and retrieved modulus of image in the TMTM case with different algorithms after 600 iterations. The original image was obtained from simulation (described in [16]). Poisson noise and white Gaussian noise with signal to noise ratio of 100 was applied to the initial intensity pattern.  $\beta$  used for HIO and RAAR were 0.7 and 0.96, respectively.

The retrieved modulus and phase of the TMTM far field after 600 iterations are presented in Figs. 3 and 4. Images were failed to be retrieved by the OSS and M-HIO algorithms alone thus are not shown here. All images reconstructed by a combination of algorithms are more accurate than that by HIO alone, suggesting that the second algorithm works to reduce the error when the

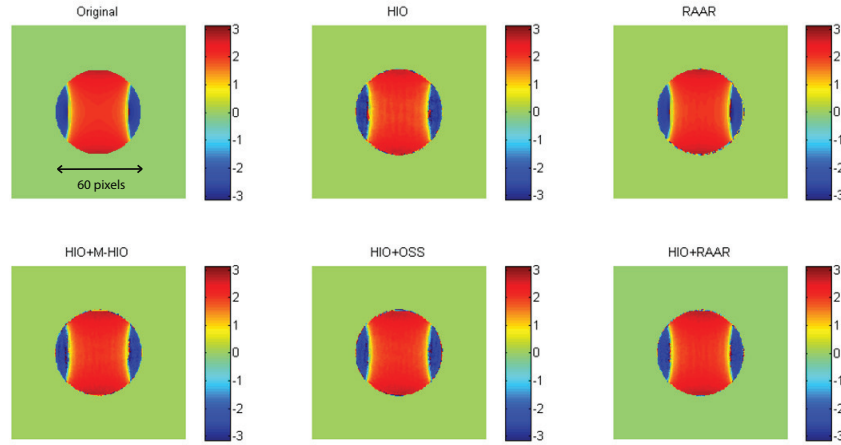


Fig. 4. The original and retrieved phase of the same images as in Fig. 3.

image is roughly constructed. In order to quantify the performance of different algorithms, we calculated the error, defined as the standard deviation from the retrieved image to the original one:

$$Error = \frac{\sum_{j=0}^m \sum_{i=0}^n |f_{ij} - cf'_{ij}|^2}{\sum_{j=0}^m \sum_{i=0}^n |f_{ij}|^2},$$

where  $i$  and  $j$  represent the positions of those pixels that contain the image,  $f_{ij}$  and  $f'_{ij}$  refer to the original and retrieved complex fields in the position  $(i, j)$  and  $c$  is a constant to compensate for the constant phase offset. The value of  $c$  is chosen such that the error is minimized, hence  $c$  is found by setting the derivative  $\frac{dError}{dc}$  equal to 0 [21], yielding

$$c^* = \frac{\sum_{j=0}^m \sum_{i=0}^n f_{ij}^* f'_{ij}}{\sum_{j=0}^m \sum_{i=0}^n |f'_{ij}|^2}.$$

As can be seen from Fig. 5, all the curves referring to combined algorithms converge faster than that with HIO and RAAR alone, as fast decrease of error at an early stage can be observed. Besides, for those curves representing combined algorithms, changes happen right after the second algorithm taking over at the 150<sup>th</sup> cycle: The red curve quickly flattens while the error stops going down. For the light blue curve, an abrupt rise of the curve is observed, followed by a smooth decline. In both cases, the curves become much smoother than all the others after around 200 iterations. Such an observation is reasonable since both the OSS and M-HIO algorithms filter considerable data outside the support and thus stabilize the image. We suppose it explains the failure of retrieval with M-HIO and OSS, that the moment the noise outside the support is filtered, some information is also lost, without which the iteration fails to converge. Finally, the purple curve representing HIO+RAAR has an abrupt drop when RAAR is applied, rendering the error reach the minimum, which is also the minimum among all the curves, at around the 250<sup>th</sup> cycle, thus we can say that it works the best in our case.

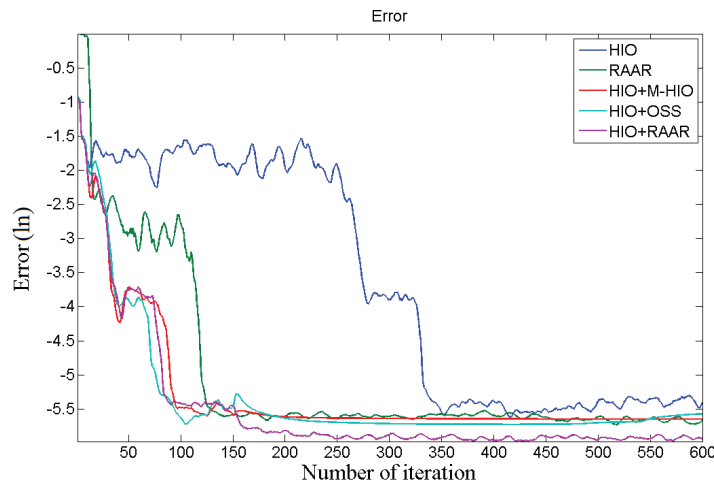


Fig. 5. The change of error of the retrieved image with iterations. This figure shows the error decline within the retrieval procedure before finally obtaining the images as shown in Figs. 3 and 4.

## 4. Experiment

### 4.1. Setup

The experimental setup is shown in Fig. 1. In our experiment, the polarized direction of the first polarizer was perpendicular (TM) to the direction of the periodic structured grating. The second polarizer can either be perpendicular (TMTE) or parallel (TMTM) to the direction of the first polarizer. Lens 3 has a focal length of 40 cm.

### 4.2. Data acquisition

As mentioned above, the intensity distribution in the focal plane of Lens 3 was measured. The BFP of Lens 2 is the plane where the complex field is to be retrieved. On the detecting plane, a CMOS camera (mvBlueFox-IGC205G, MATRIX VISION GmbH) with  $2592 \times 1944$  pixels with pixel area of  $2.2\mu\text{m} \times 2.2\mu\text{m}$  was placed to capture the intensity of the targeted field.

Before recording the data from the grating, the part of the silicon wafer without the grating was illuminated and the reflected light, which was collimated and thus regarded as a plane wave was recorded by the camera. Next, the sample with a grating structure perpendicular to the polarization directions of both two polarizers was illuminated and the diffraction pattern of the TMTM field was recorded. Lastly, the second polarizer was rotated  $90^\circ$  and the image of the TMTE field was recorded.

Since the measurement was taken at the focal plane, the diffraction patterns are highly focused and consequently, the signal of the side lobes decays fast below the noise level. Limited by the finite dynamic range of the camera, high-frequency signals were lost during the sampling procedure. Therefore, images with different exposure times were recorded and combined to provide an effective increase in the dynamic range of the camera. We show an over-exposed intensity pattern exposed for  $76000\mu\text{s}$  in Fig. 6(a), and along the red line we plot the intensity distributions of images obtained with different exposure times in Fig. 6(b). Our reconstruction is based on that the intensity ratio between the baseline (the sample region in Fig. 6(b)) and any point of the same image should be a fixed value, as suggested in Fig. 6(c), which shows the ratio of the intensity distribution along the green line to that of the sample region in the same image. All those curves obtained with different exposure times nearly overlap, and we infer that the

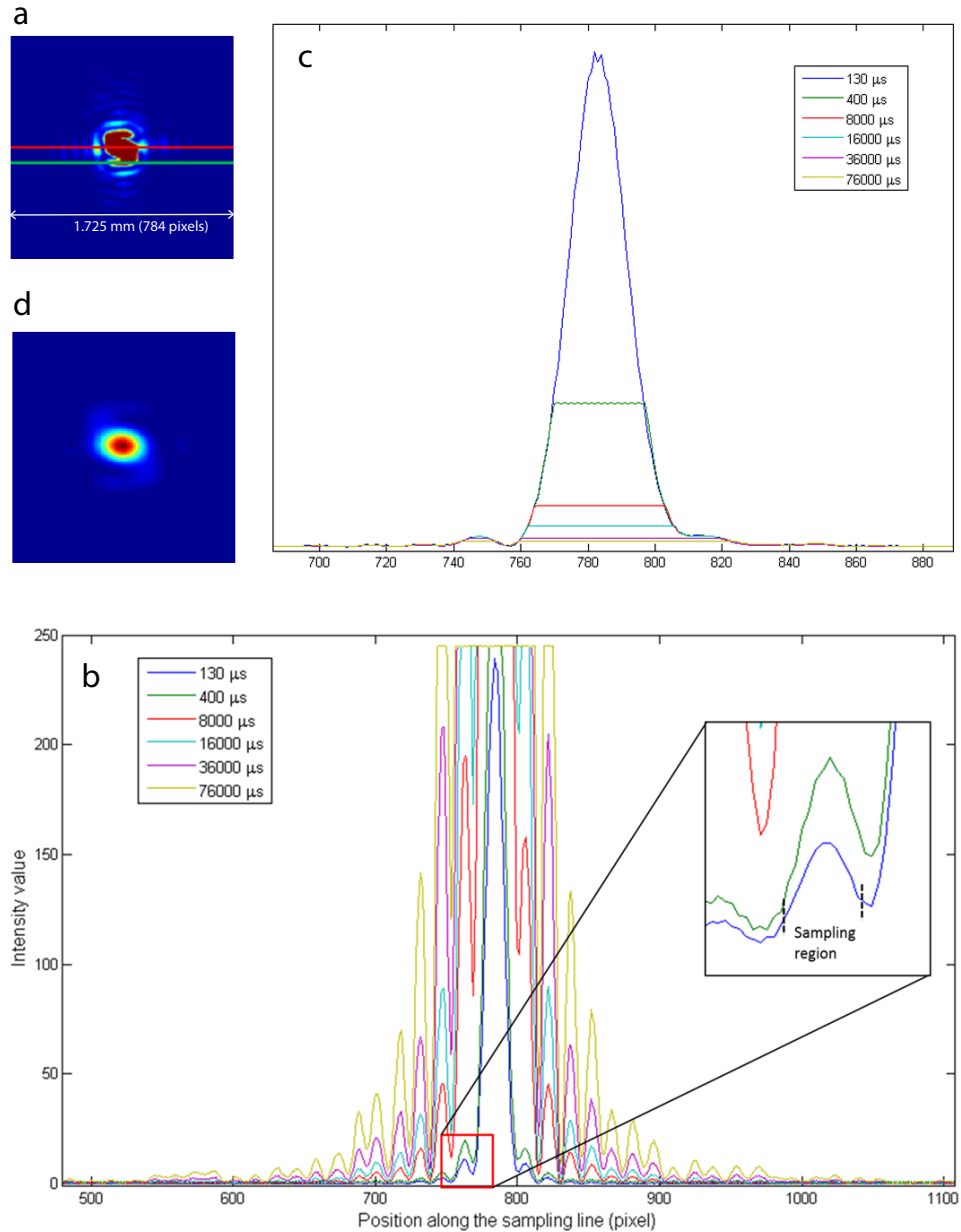


Fig. 6. (a) intensity profile of the TMTM field exposed for  $76000\mu\text{s}$ . The red part in the center denotes strong over-exposure; (b) cross sections of images taken at different exposure times. The cross section is taken following the red line as shown in (a); (c) the relative intensity ratio of the cross section denoted as the green line in (a) to the sample region as in (b) for a given exposure time. (d) the reconstructed image.

over-exposed part (flat lines in the middle) should also follow the same trend, and thus can be reconstructed. Following this method we obtain the reconstructed intensity pattern as shown in Fig. 6(d).

#### 4.3. Phase retrieval from reconstructed intensity patterns

As is suggested by the simulation results, the combination of HIO and RAAR works the best to stabilize the solution and reduce the error from noisy data. Therefore, RAAR was applied following the HIO algorithm, with changes in  $\beta$  and the number of iterations. For the image in the Fourier domain, four neighboring pixels were merged to be one pixel in order to reduce the running time of the program. This procedure, known as binning, also leads to an increase of the signal to noise ratio. The total field has  $784 \times 784$  pixels and the size of the support was found to be  $54 \times 54$  pixels.

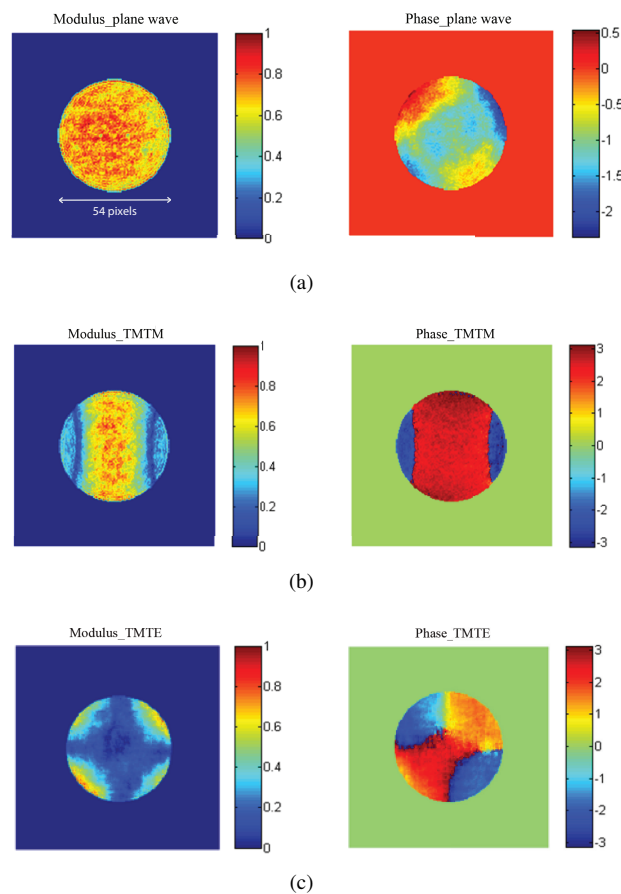


Fig. 7. Retrieved modulus and phase of (a) plane wave, (b) TMTM and (c) TMTE images from the combination of HIO and RAAR algorithms. For retrieval of plane wave, HIO with  $\beta$  of 0.98 was performed for 250 iterations, followed by RAAR, with  $\beta$  of 0.96, for the next 250 iterations. The same parameters were applied for the retrieval of image in the TMTM case. To reconstruct the image in the TMTE case however, HIO was applied twice with different  $\beta$ : firstly  $\beta = 0.9$  was used for the first 150 iterations, followed by  $\beta = 0.96$  for the next 100 iterations, and lastly RAAR was applied with  $\beta = 0.96$  for the remaining 250 iterations.

Our best retrieved modulus and phase of the images at the pupil are shown in Fig. 7. Figure 7(a) refers to the plane wave case, which ideally should have uniform modulus and zero phase, however, due to aberrations that are present in our optical system and also imperfection of the beam, the modulus of the image is non-uniform and the phase is curved. In the retrieval of the TMTM and TMTE fields, such discrepancy in the input field has been corrected.

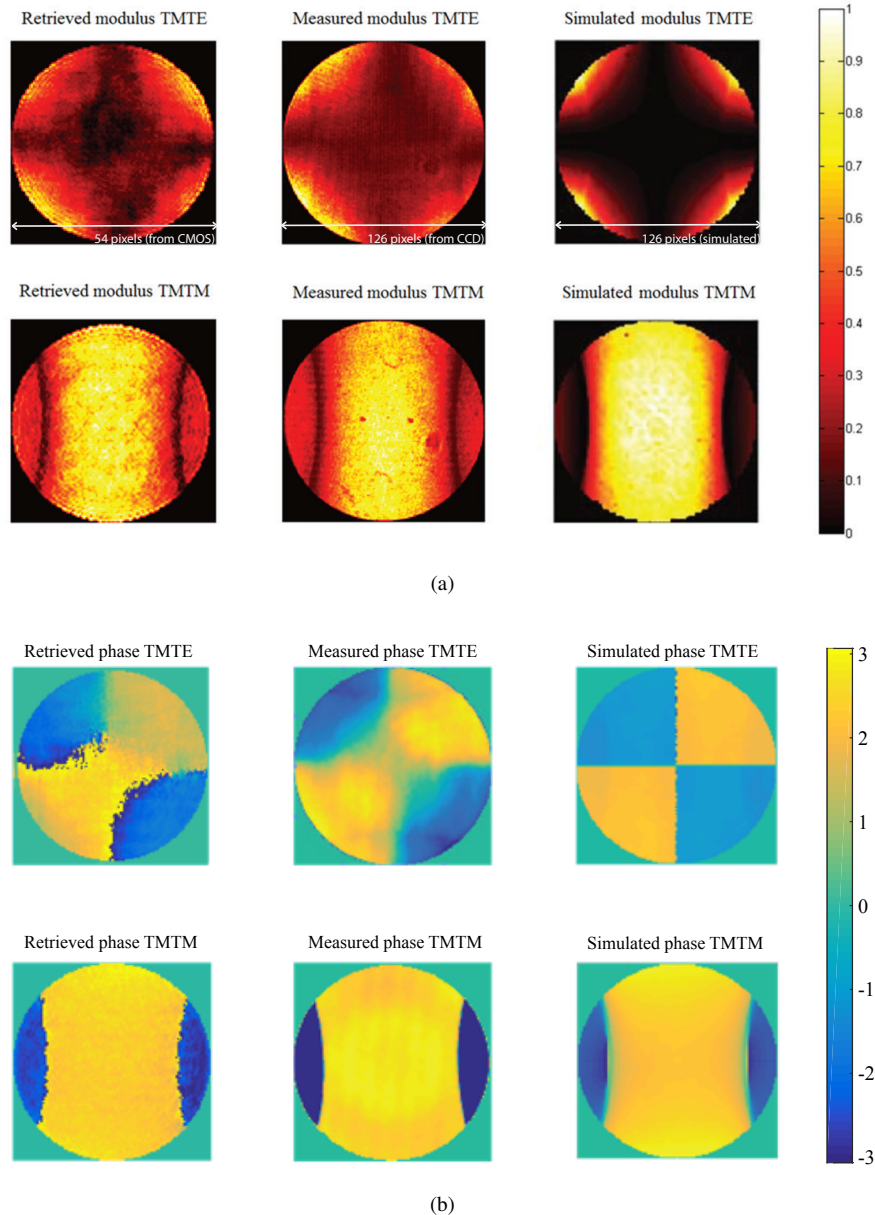


Fig. 8. Comparison of (a) modulus and (b) phase of images obtained from phase retrieval, interferometric measurement and simulation (the latter two cases are reproduced from [16]).

For retrieval of the plane wave, HIO with  $\beta$  of 0.98 was performed for 250 iterations, followed by RAAR, with  $\beta$  of 0.96, for next 250 iterations. The same parameters were applied for the

retrieval of the image in the TMTM case. To reconstruct the image in the TMTE case however, HIO was used twice with different  $\beta$ : firstly HIO with  $\beta = 0.9$  was used for the first 150 iterations, followed by HIO with  $\beta = 0.96$  for the next 100 iterations, and lastly RAAR with  $\beta = 0.96$  for the remaining 250 iterations. Such a sequence has been chosen because it was found that the phase retrieval tends to be more stable and accurate as  $\beta$  approaches 1; however, if  $\beta$  is very large at the beginning, the algorithm is very likely to fail.

In order to test the accuracy of the retrieved images, the images in the TMTM and TMTE cases obtained by phase retrieval are compared with that from the direct measurement of the phase using interferometry as well as from simulations [16], as shown in Fig. 8. The retrieved result successfully reproduces the main features of the simulated and interferometrically measured far fields. Note that the images in the second column are moduli measured with a CCD camera with a different pixel size, thus have different pixel numbers. Images in the third column were simulated with the same parameters.

Another observation that needs to be mentioned here is that the retrieved and directly measured modulus and phase of both the TMTM and TMTE cases share more similarities with each other than with the simulated ones. One possible reason is that the simulated complex image at the pupil is not a realistic model for the real case, since the simulation is based on the measured parameters of the grating and nominal parameters (side wall angle), which may not be accurate. Besides, other factors such as aberrations of lenses and the scattered light from other optical surfaces can lead to the deviation of the experimental result from the ideal case. Further, in practice, it is very difficult to realize the ideal TMTE case since even when the polarized directions of the two polarizers are perpendicular to each other, light cannot totally cancel out; this is due to the finite extinction ratio of the polarizer and/or very tiny error in the angle adjustment of the polarizer. Also, since the light intensity is very low in the TMTE case, the effect of stray light cannot be neglected.

## 5. Conclusion

In conclusion, we presented here an analysis of various phase retrieval methods applied to retrieve the complex far field from a grating that is illuminated by a focused laser beam. The knowledge of the phase of the far field can be used as extra information for the problem of grating reconstruction that finds application in quality inspection in optical lithography. Our method is more robust and easy to apply than interferometry, since in our case, there is no reference mirror, no moving parts and the system is not susceptible to vibrations. Our results are compared with rigorous simulations and with phase measurements obtained with interferometry. Although the main goal here was the application in optical inspection in lithography, we believe that this technique could be applied in other applications regarding reconstruction of nanostructures where the phase information can have added value.